# Contrast Mechanism of Osmium Staining in Electron Microscopy of Biological Tissues

Ruiyu Li,<sup>†,‡</sup> Gregg Wildenberg,<sup>¶</sup> Kevin Boergens,<sup>§,¶</sup> Yingjie Yang,<sup>§</sup> Kassandra Weber,<sup>§</sup> Janek Rieger,<sup>‡</sup> Ashley Arcidiacono,<sup>‡</sup> Robert Klie,<sup>§</sup> Narayanan Kasthuri,<sup>†,¶</sup> and Sarah B. King\*,<sup>†,‡</sup>

†Department of Chemistry, University of Chicago, Chicago, IL, USA ‡James Franck Institute, University of Chicago, Chicago, IL, USA ¶Department of Neuroscience, University of Chicago, Chicago, IL, USA §Department of Physics, University of Illinois Chicago, Chicago, IL, USA

E-mail: sbking@uchicago.edu

#### Abstract

Electron imaging of biological samples stained with heavy metals has enabled visualization of nanoscale subcellular structures critical in chemical-, structural-, and neuro-biology. In particular, osmium tetroxide has been widely adopted for selective lipid imaging. Despite the ubiquity of its use, the osmium speciation in lipid membranes and the mechanism for image contrast in electron microscopy (EM) have continued to be open questions, limiting efforts to improve staining protocols and improve highresolution imaging of biological samples. Following our recent success using photoemission electron microscopy (PEEM) to image mouse brain tissues with a subcellular resolution of 15 nm, we have used PEEM to determine the chemical contrast mechanism of Os staining in lipid membranes. Os (IV), in the form of OsO<sub>2</sub>, generates aggregates in lipid membranes, leading to a strong spatial variation in the electronic structure and electron density of states. OsO<sub>2</sub> has a metallic electronic structure that drastically increases the electron density of states near the Fermi level. Depositing metallic OsO<sub>2</sub> in lipid membranes allows for strongly enhanced EM signals of biological materials. This understanding of the membrane contrast mechanism of Os-stained biological specimens provides a new opportunity for the exploration and development of staining protocols for highresolution, high-contrast EM imaging.

#### Introduction

Osmium tetroxide has been extensively used as a lipid-specific stain for enhancing membrane contrast in electron microscopy for the last few decades. The successful development of a reliable heavy-metal staining protocol for biological material has facilitated electron microscopy imaging of biological systems with subcellular resolution using scanning electron microscopy (SEM) and transmission electron microscopy (TEM).<sup>2-6</sup> OsO<sub>4</sub> staining is routinely used in a variety of fields ranging from fundamental chemistry, 7,8 biology, <sup>1,9,10</sup> and medicine research <sup>11</sup> to histology of pathological tissue during medical diagnostics and treatment. 11-13 Despite the prevalent and widespread adoption of osmium staining in electron microscopy, the nature of the contrast mechanism in EM, as well as the molecular reactions required for the staining process, are surprisingly unknown.

Conventional understanding of the mechanism of Os contrast in EM generally focuses on the identity of Os as a "heavy metal", with a

large atomic number. <sup>14</sup> Historically, the biological literature suggested that osmate esters are formed in the tails of unsaturated fatty acids in lipid membranes, as facilitated by the wellunderstood reaction of OsO<sub>4</sub> with alkenes. <sup>15</sup> The increased electron density afforded by the Os(VIII) species in the membranes was suggested to be the source of improved electron scattering and electron interactions in SEM and TEM in regions of biological material with high lipid concentrations. More recently, research on improving the staining of whole brain samples for neuroscience applications hypothesized the osmium species responsible for EM contrast is osmium (IV) (OsO<sub>2</sub>), rather than the previously proposed osmium (VIII) (osmate ester). Upon staining, the biological material underwent an observable color change in an ex situ model experiment, suggestive of the formation of Os(IV). 9 However, the presence of OsO<sub>2</sub> was not confirmed and no explanation was provided for how contrast is generated by OsO<sub>2</sub>. X-ray photoelectron spectroscopy (XPS) of stained specimens showed the presence of a mixture of low Os oxidation states, but lacked the spatial resolution needed to determine the location of different Os oxidation states. 16 Without a fundamental understanding of what molecular species exist during the staining process and what role they play in image contrast, efforts to improve image contrast in EM of biological materials are limited to exhaustive search rather than rational designs. This makes it particularly challenging to assess modified staining protocols. Furthermore, without a clear grasp of the source of imaging contrast, developing alternatives to highly toxic osmium tetroxide remains unobtainable.

We have recently demonstrated successful wide-field imaging of ultra-thin brain slices (UTBS) with 15 nm resolution using a technique named photoemission electron microscopy (PEEM). <sup>17</sup> PEEM is based on photoelectric effect where a UV photon excites a material that then can emit electrons that are then magnified and mapped to a detector using electron optics analogous to the magnification of photons in wide-field light microscopy, as shown in Figure 1(a). As the diffraction

limit of electrons is on the order of Å rather than 100s of nm, PEEM allows for material imaging with spatial resolution as good as 8 nm. <sup>18</sup> PEEM has been rigorously developed for probing electronic properties of flat material samples including metals, 19,20 two-dimensional semiconductors<sup>21–24</sup> and polymer films.<sup>25</sup> In these systems, the contrast results from a spatially varying work function, and/or differences in electronic structure and density of states (DOS). As such, high-quality PEEM imaging generally requires materials that are conductive - metals or high-mobility semiconductors. Biological materials are conventionally thought of as insulating materials and are challenging to image with PEEM.<sup>26</sup> Contrary to this understanding, we obtain synaptic resolution PEEM images of UTBS stained with the same staining protocol developed by Hua et al. that has been previously used in SEM imaging. 9,17 Following our initial study, it was a puzzle to us how high-resolution and high-contrast images could be generated from insulating biological samples.

In this paper, we show that biological materials stained with  $\mathrm{OsO_4}$  and  $\mathrm{K_4Fe}(\mathrm{CN})_6$  contain OsO<sub>2</sub>in lipid membranes. <sup>27,28</sup> OsO<sub>2</sub> behaves like a metal, possessing a high electronic density of states that crosses the Fermi level, and provides the needed conductivity and electronic density of states for successful PEEM imaging of biological tissues. We propose a full mechanistic picture leading to OsO<sub>2</sub> formation, discuss possibilities for a likely slow step, and pinpoint specific routes for contrast improvement. As the speciation of osmium also plays an important role in the contrast of SEM and TEM that share the same staining protocol, the mechanism of Os staining and image contrast described here is equally critical for improving the image quality of biological materials in the broader EM field.

## **Experimental Methods**

Mouse brain sections were prepared for PEEM imaging following the same protocol used for SEM<sup>9</sup> and for PEEM imaging in our previous

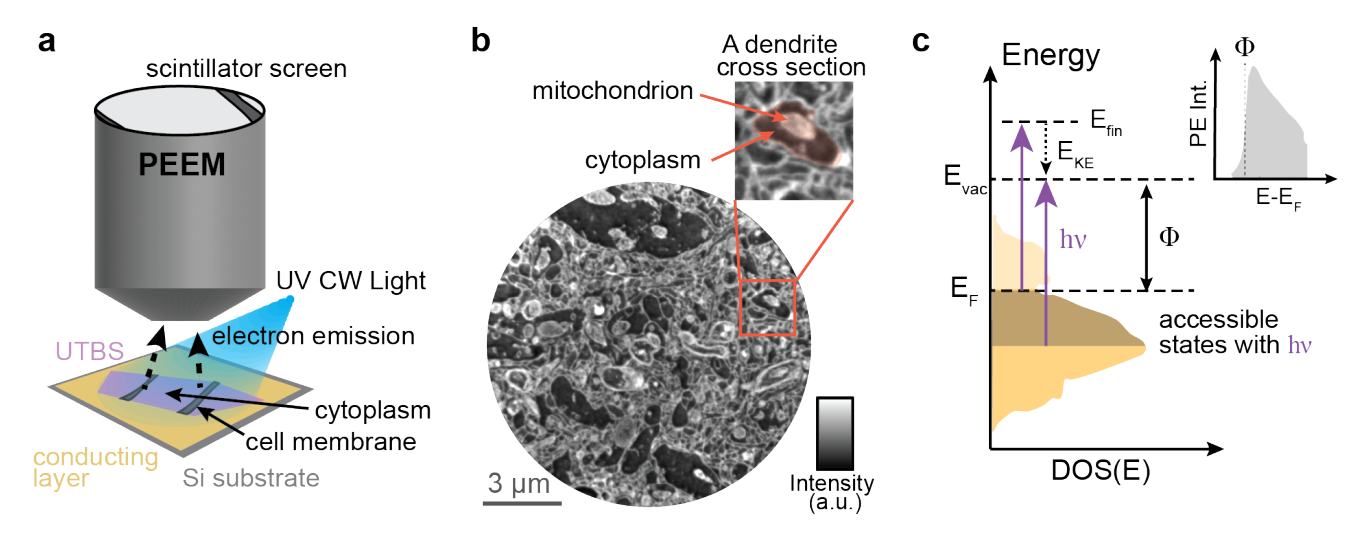


Figure 1: (a) A schematic of PEEM. A ultra-thin brain slice (UTBS) is on a gold-coated Si substrate, illuminated by a Hg lamp UV continuous-wave (CW) light source. (b). A representative PEEM image of mouse brain tissue. The bright contours indicate cell membrane stained with osmium, and the dark features are cytoplasm. Ultrastructure can be clearly revealed, such as the neural dendrite and the mitochondrion in the shaded area in the inset. (c) Energy diagram of photoemission process, where electrons in occupied states below the Fermi level ( $E_F$ ) are photoexcited with UV light of photon energy  $h\nu$  to a final states ( $E_{fin}$ ) above vacuum level ( $E_{vac}$ ) with kinetic energy  $E_{KE}$ . The work function,  $\Phi$ , is the energy difference between  $E_F$  and  $E_{vac}$ . Inset shows a schematic of the obtained photoemission spectrum from the accessible density of states (DOS) as a function of kinetic energy of photoelectrons.

work using "reduced osmium" staining protocol. 17 Briefly, the mouse was perfused transcardially to preserve tissue ultrastructure. mouse brain was surgically removed and fixed, and a vibratome sectioned brain slice (200 – 300 µm) was stained with successive rounds of osmium tetroxide and potassium ferrocyanide before ethanol dehydration and embedding with EPON resin. Resin encapsulated brain was then sectioned using an ultramicrotome to a 40-80 nm-thick UTBS which was picked up on a Si substrate with native oxide  $(n-SiO_2/Si)$  coated with 50 nm of polycrystalline gold. The additional conductive layer is used to prevent sample charging during photoemission.<sup>29</sup> Further details of sample preparation can be found in the Supporting Information.

The UTBS on the  ${\rm Au/n\text{-}SiO_2/Si}$  substrate is illuminated using a broadband Hg arc lamp that generates ultra-violet (UV) continuous-wave (CW) light, shown schematically in Figure 1(a). The lamp is mounted with a high-pass optical filter allowing photons with energies greater than 4.43 eV (280 nm) to im-

pinge on the sample, and the highest photon energy is about 5.0 eV (247nm) (see full spectrum in Figure S3). The resulting photoelectrons are imaged with a photoemission electron microscope manufactured by Focus GmbH. The PEEM operates at ultra-high vacuum (UHV,  $10^{-11}$  mbar). Photoexcited electrons are accelerated by a 12 kV potential applied normal to the sample plane, focused via a series of electron lenses in the PEEM onto a single microchannel plate (MCP), converted to visible light by a phosphor screen, and eventually imaged by a CCD camera. The typical exposure time for one image is 10 seconds. High-resolution images are obtained by averaging the same regions of interest (ROI) to improve signal-to-noise (S/N). The PEEM is equipped with a high-pass energy filter where only photoelectrons with kinetic energies higher than a given energy threshold can pass and be detected. The energy resolution of the instrument is approximately 50 meV and scans were collected using 100 meV steps.

Additional characterization was done using scanning transmission electron microscopy

(STEM, JEOL ARM200-CF). The chemical composition of the Os-stained region was analyzed with energy dispersive spectroscopy (EDS, Oxford XMAX100TLE) to determine the Os:O ratio. A total exposure time of up to 15 minutes was used during EDS measurements due to the thin nature of the specimen. Electron energy-loss spectroscopy (EELS, post-columns Gatan Continuum GIF ER spectrometer) measurements were conducted on osmiumrich regions as well, with an electron probe semi-convergence angle of 17.8 mrad and a collection angle of 53.4 mrad.

#### Results and Discussion

Figure 1(b) shows a PEEM image of a UTBS on a Au/n-SiO<sub>2</sub>/Si substrate. Photoelectrons are emitted from the UTBS via a one-photon photoemission process with UV illumination. Brighter regions of Figure 1(b) indicate more photoemissive components whereas darker regions are biomaterials that have low photoemission yield. Based on comparison to SEM images of similar samples, the bright outlines depict the membranes of neurons or organelles that selectively bind osmium. The darker background consists of unstained regions of biological tissues, such as cytoplasm, that do not contain lipid bilayers. More specifically, the inset of Figure 1(b) is the zoom-in of the red box. The shaded region is the cross-section of a neural dendrite, and the bright solid spot within the cytoplasm is a mitochondrion. The difference in signal intensities allows us to visually distinguish the ultrastructure of biological material with subcellular resolution, and the features are comparable to what has been previously collected using SEM.<sup>30</sup>

The contrast observed in PEEM is due to stained and non-stained regions generating different intensities of photoelectrons. To understand why photoemission intensity varies spatially in the brain tissue, we performed energy-resolved PEEM to measure the local electronic structure of the UTBS. We used a high-pass energy filter to incrementally cut out photoelectrons with kinetic energy lower than an energy

threshold and obtained a series of PEEM images at the same sample position. The photoemission intensity of an ROI is extracted as a function of energy, and we compute the energy distribution of the photoelectrons by performing a numerical differentiation of the energyresolved images (see Supporting Information for the details). To a first approximation, this energetic distribution represents the electronic structure of the occupied electronic states below the Fermi level. The low energy edge of the distribution, termed the secondary edge in the photoemission spectroscopy literature, is a measure of the material work function, <sup>31,32</sup> which describes the lowest energy an electron needs to overcome the vacuum barrier and be ejected from the material. This value is depicted as the energy difference between the vacuum level and the Fermi level ( $\Phi = E_{vac} - E_F$ ) in the energy diagram in Figure 1(c).

Figure 2(a, inset) shows three ROIs of varying signal intensities and their corresponding photoemission spectra. All three curves have been normalized to the peak intensities and offset vertically for clarity. The energy axis  $(\Delta(E_{\text{vac}}-E_{\text{F}}))$  is calibrated to the secondary edge of the spectrum from the brightest area (top spectrum). Despite variation in the total photoemission counts, the three spectra display almost identical photoemission spectra. We can estimate the relative work function  $(\Delta\Phi)$  of each region with respect to the brightest ROI from half of the maximum magnitude of the secondary edge in the photoemission spectrum. The dashed line in Figure 2(a) marks the secondary edges of the three spectra, which are the same within  $\pm 0.05$  eV (instrument resolution). This result indicates that there is no work function variation across the sample even with the existence of heavy metal stains. Therefore, the image contrast that is observed with UTBS in both PEEM and SEM cannot be due to sample work function variation, but must be due to a variation in the sample electronic structure.

Electronic structure differences, as the other primary contrast mechanism in PEEM, are either due to the spatial variation of the electronic structure of a sample or a spatial variation in a chemical species concentration. The

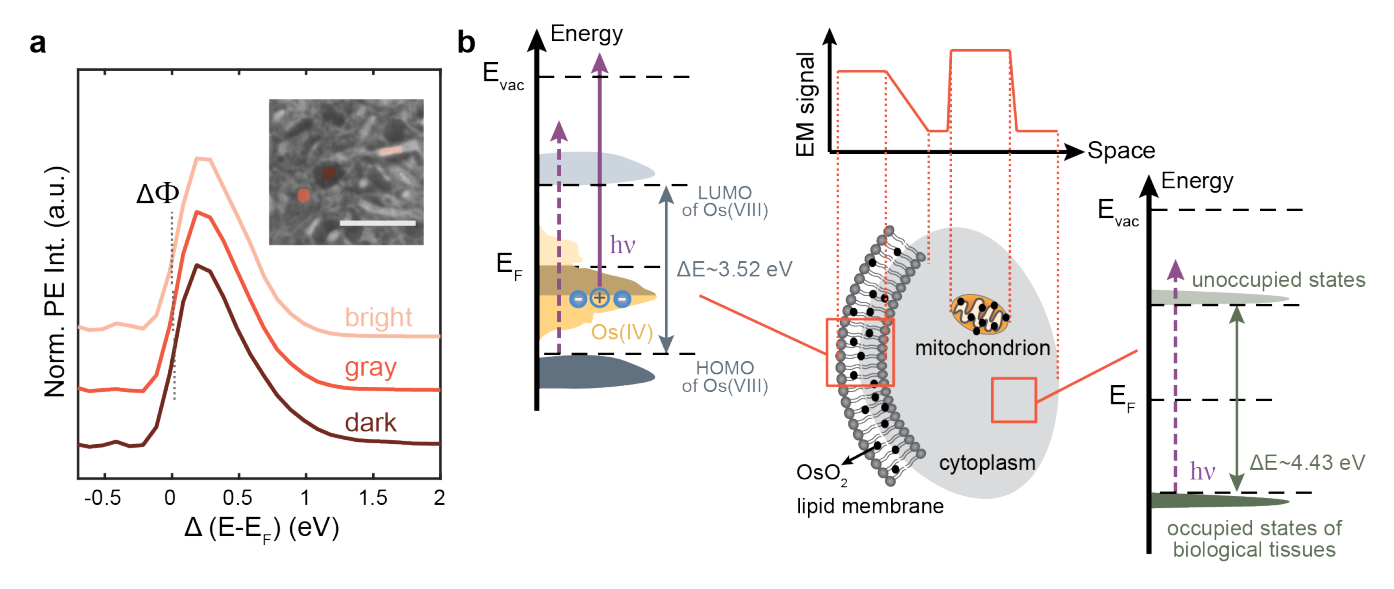


Figure 2: (a) Photoemission spectra of bright, gray and dark ROIs showing in the inset. Dashed lines indicate work function relative to the secondary edge of the spectrum corresponding to the brightest region. Scale bar is 2  $\mu$ m. (b) Energy diagrams comparing electron densities of osmium(VI) near the Fermi level with HOMO-LUMO gaps of Os(VIII) and biological tissues. Lipid membranes of cells and organelles such as mitochondria efficiently bind to osmium, generating stronger signals in EM images, whereas unstained regions such as cytoplasm generally have low EM intensity.

high energy sides of the photoemission spectra in Figure 2(a) are virtually identical. The similarity in spectra makes it unlikely that we have a spatial variation in the material electronic structure. It is instead more likely that there exists spatial variation in the concentration of chemical species that results in distinct photoemission intensity. In this instance, the contrast results from a spatial variation of osmium species. As shown schematically in Figure 2(b), biological tissues, such as unstained cytoplasm, do not have well-defined electronic structure due to their chemical complexity, and typically are considered to be insulating materials. For example, proteins commonly have an extremely large optical bandgap around 4.43 eV (280 nm).<sup>33</sup> Therefore, the photon source used herein can not photoemit efficiently from the occupied electronic states of pure biological tissues, resulting in low photoemission intensities. Similarly OsO<sub>4</sub> and Os(VIII) compounds are also insulators with large HOMO-LUMO gaps, of 3.52 eV ( $\approx 352 \text{ nm}$ ), <sup>34</sup> resulting in low photoemission yield. However,  $OsO_2$  is known to have metallic characteristics, <sup>27,35</sup> providing OsO<sub>2</sub> with the requisite electronic structure to induce high photoemission signals.

Similar to its well-studied Group 8 analog RuO<sub>2</sub>, OsO<sub>2</sub> tends to crystallize in a rutile structure, resulting in metal oxide aggregate formation. <sup>27,28,36</sup> Figure 3(a) shows a high-angle annular dark-field transmission electron microscopy (HAADF-STEM) image of UTBS on a TEM grid, where the bright contrast corresponds to atomic columns containing elements with high atomic number. Bright contrast in the HAADF image shows aggregates clustering along cell membranes. EDS mapping of the same ROI (Figure 3(b)) shows that the bright aggregates are osmium-rich, confirming that osmium has indeed been deposited specifically in the lipid membranes. Figure 3(c) shows the corresponding EDS spectrum. Characteristic peaks of osmium M and L $\alpha$  at 1.91 keV and 8.91 keV, respectively, can be clearly observed, and oxygen  $K\alpha$  signal is also confirmed at 0.525 keV. The average elemental ratio of Os:O from the Os-rich areas is calculated to be between 1:2 to 1:3, corroborating  $OsO_2$  as the main osmium species. It is important to note that O signal is also detected in background areas where there is limited contrast from the bright clusters, indicating the likely overestimation of O composition in Os-O compounds. Furthermore, we

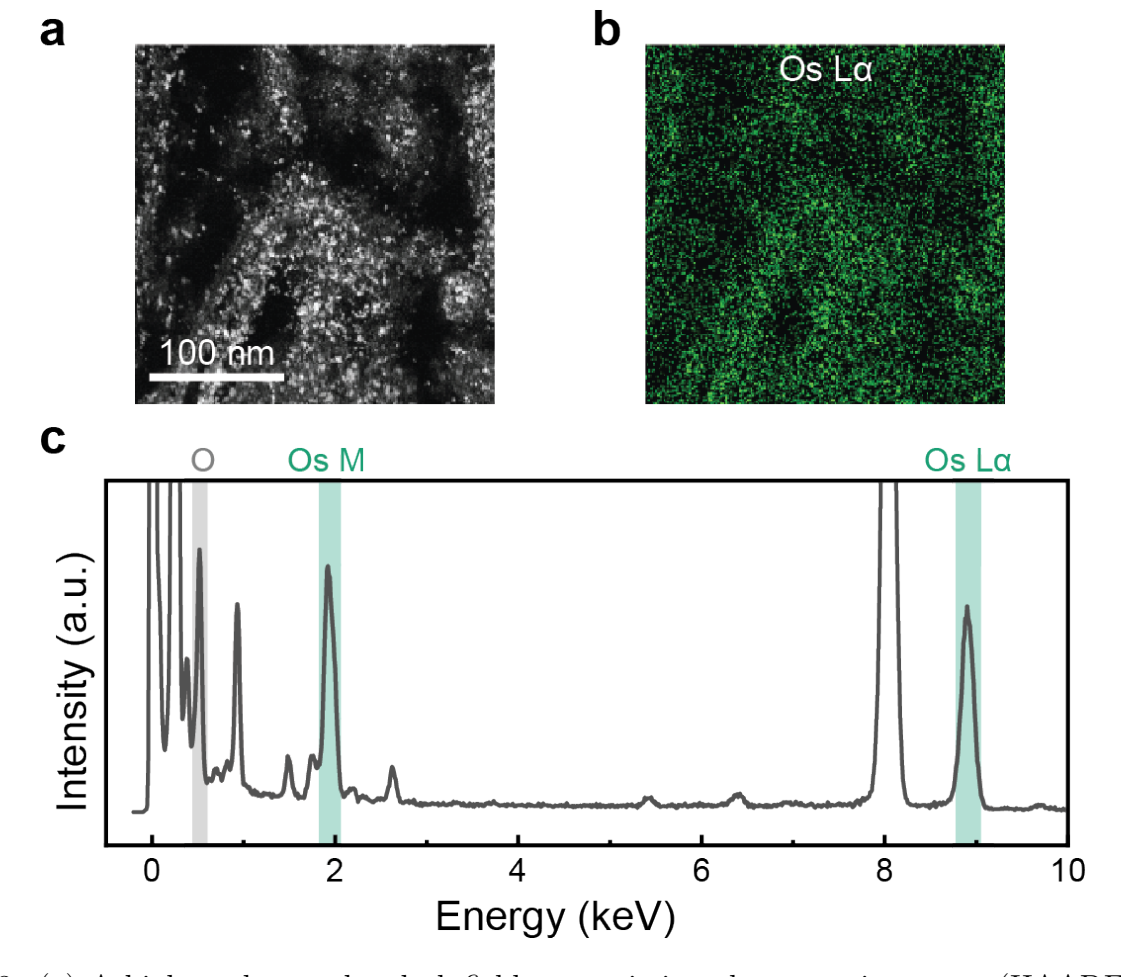


Figure 3: (a) A high-angle annular dark-field transmission electron microscopy (HAADF-STEM) image of an area with clear contrast of aggregates along cell membranes. (b) EDS map from the Os L $\alpha$  signal of the mapped area. (c) EDS of the elements detected, where the grey band highlights the O K signal at 0.525 keV, and green bands highlights Os M and L $\alpha$  peaks at 1.91 keV and 8.91 keV, respectively. Note that other elements were also detected in the spectrum, but were disregarded for the purpose of the analysis.

used electron energy loss spectroscopy (EELS) to additionally verify the existence of both Os and O(see more discussion in the Supporting Information). The combination of the EDS and EELS results indicates that Os most likely takes the valence state of IV, despite that some mixture of higher and lower states of osmium persists. <sup>16,37</sup>

Hua et al. considered the formation of OsO<sub>2</sub> in tissue stains based on color comparisons in a test tube experiment and proposed a simple reaction scheme that invites future experiments to prove the contributions of low-oxidation state osmium in EM staining. Here, having confirmed OsO<sub>2</sub> and Os(IV) compounds as primary chemical species that provide both

PEEM and SEM contrast, we aim to provide a more detailed and accessible description of the staining mechanism.

Buffered  $OsO_4$  is introduced to biological tissue in its ionic water-soluble form,  $[OsO_4(OH)_2]^{2-}$ , see Step 1 in Figure 4. To ensure homogeneous staining across 100s  $\mu m$ -thick tissue block, osmium compounds passively diffuse through various layers of membranes to penetrate cells and organelles. This process is facilitated by  $[OsO_4(OH)_2]^{2-}$  switching back and forth with its non-polar lipophilic form  $OsO_4$ , losing or gaining two hydroxyl groups at the membrane-cytoplasm interface, resulting in even distribution of Os(VIII) in the cell lipid phase.

In the next step (Step 2),  $OsO_4$  selectively couples to specific sites in the lipid membranes to form bound osmium. It is widely accepted that this process is realized via Sharpless dehydroxylation, where C=C bonds in unsaturated fatty acids attack an electropositive osmium center of the Os=O, resulting in the formation of an intermediate cyclic osmate ester.  $^{16,37,38}$  This ultimately leads to the reduction of Os(VIII) to Os(VI), as verified previously by XPS measurements.  $^{16}$ 

The transiently generated Os(VI) in Step 2 can be accessed through two different pathways, either via the migration of the osmate ester to the hydrophilic head of the lipids for spontaneous hydroxylation (Pathway I in Figure 4), or via reduction, initiated by additive  $K_4$ Fe(CN)<sub>6</sub>, producing water-soluble  $[OsO_2(OH)_4]^{2-}$  in the aqueous phase (Pathway II). In Pathway I, nearby water molecules or hydroxyl groups are necessary to promote hydroxylation (Step 3), but their origin in the lipid phase has been vaguely discussed in the literature. It is known that water can passively diffuse across lipid membranes to allow for osmotic equilibrium; this small population of water may serve as a potential –OH source in the membrane.<sup>39</sup> Additionally, it has been observed that osmium can migrate towards the membrane-water interface, resulting in a higher concentration of osmium complexes at the hydrophilic heads. 16,40 This may be in part due to interfacial water facilitating the ring-opening reaction. Finally, hydroxyl groups in the phospholipids can be also utilized to form  $[OsO_2(OH)_4]^{2-}$ .

In the second pathway, Os (VIII) can also be reduced via the addition of a reducing agent, in this work potassium ferrocyanide ( $K_4Fe(CN)_6$ ).  $[OsO_4(OH)_2]^{2-}$  is directly reduced outside the lipid bilayer to Os(VI) (Step 4) in parallel with the spontaneous hydroxylation that occurs in Pathway I. This reduction step circumvents the osmate ester formation between the bilayer and greatly accelerates the generation of Os(VI) in the aqueous phase.

In the end, the formation of  $OsO_2$  occurs via a disproportionation reaction of Os(VI) under biological pH conditions (buffer pH=7.4). <sup>16,41</sup> Previous X-ray studies of model systems sug-

gested the presence of a dimeric Os(VI) crystal structure with a double oxo bridge.  $^{16,42}$  Herein, we assume that the same dioxo-bridged osmium species is being formed under biological conditions (Step 5).  $^{36}$  The hexavalent osmium complex is known to be unstable and undergoes asymmetric Os–O bond cleavage, leading to the oxidation of one Os(VI), regenerating Os(VIII), and the reduction of the other Os(VI) center, forming  $[OsO_2(OH)_2]^{2-}$  in water (Step 6).  $^{43}$  The dehydroxylation of  $[OsO_2(OH)_2]^{2-}$  can readily deposit the lipid-soluble OsO<sub>2</sub> into the bilayer membranes as aggregates (Step 7), resulting in the primary contrast observed in EM images.

Our determination of the end product of the reduced osmium staining protocol goes beyond PEEM. Other EM techniques that are commonly used for biological imaging, such as SEM and TEM, adopt the same staining method and will significantly benefit from the proposed reaction mechanism. With the understanding of the speciation of osmium stain, efforts can be made towards the deposition of a higher concentration of OsO<sub>2</sub> into the lipid membranes. For example, the possibilities to initiate Pathway I in Figure 4 suggest that finding new ways to introduce -OH in proximity to membrane heads could potentially increase the production of  $[OsO_4(OH)_2]^{2-}$  for the eventual generation of the contrast relevant OsO<sub>2</sub>. Overall, the contrast mechanism of osmium staining promotes intentional modifications for protocol development rather than attempts based upon exhaustive searches.

## Conclusion

In summary, this paper provides a detailed description of the contrast mechanism of Osstained ultra-thin brain slices in electron microscopy. Previously thought to be unachievable, we demonstrate the successful high-contrast imaging of insulating, biological material with PEEM for the determination of the staining mechanism. Energy-resolved PEEM measurements show a negligible difference in nanoscale work function across the sample sur-

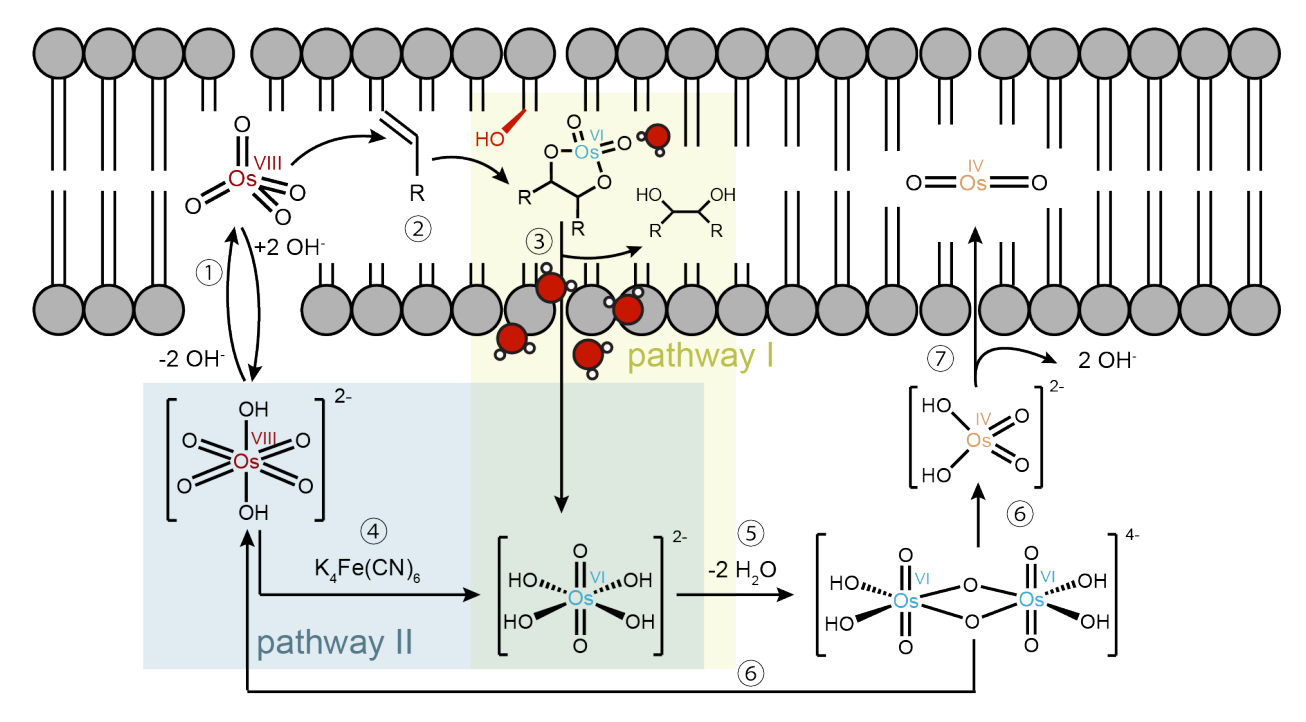


Figure 4: Schematic illustration of the formation and deposition of  $OsO_2$  in the lipid membrane during the staining process.

face, indicating, for the first time, that the contrast in Os-stained biological samples in PEEM originates from differences in the electronic density of states for Os compounds compared to the surrounding biological tissues. We also determine that  $OsO_2$  is likely the main source of EM contrast, due to its metallic electronic structure. This finding was consistent with the appearance of OsO<sub>2</sub> aggregates in STEM of UTBS and elemental ratios from EDS mapping of UTBS. Finally, we proposed a full and detailed scheme of the reactions and pathways necessary for the formation of  $OsO_2$  in the lipid membranes. The determination of the source of contrast, as well as the relevant pathways for OsO<sub>2</sub> generation suggested herein challenges the long-adopted understanding of Os-staining. Our proposed mechanism sets the chemical foundation for improving staining protocols for biological imaging using not only PEEM but also other EM techniques including TEM and SEM, ultimately enabling faster and higher resolution electron microscopy imaging.

Acknowledgement This work made use of the shared facilities at the University of Chicago Materials Research Science and Engineering Center, supported by National Science Founda-

tion under award number DMR-2011854. R.L. acknowledges support from MRSEC Graduate Fellowship (DMR-2011854). S.B.K. acknowledges start-up funding support from the University of Chicago and the Neubauer Family Assistant Professors Program. This work was supported in part by funding from the NSF (award No.2207383 and No.2014862). YY and RFK research was supported by the Army Research Office and was accomplished under Grant Number W911NF-23-1-0225. The views and conclusions contained in this document are those of the authors and should not be interpreted as representing the official policies, either expressed or implied, of the Army Research Office or the U.S. Government. The U.S. Government is authorized to reproduce and distribute reprints for Government purposes notwithstanding any copyright notation herein. This work made use of instruments in the Electron Microscopy Core at the UIC Research Resources Center. The acquisition of UIC JEOL JEM ARM200CF is supported by an MRI-R<sup>2</sup> grant from the National Science Foundation (Grant No. DMR-0959470) and the upgraded Gatan Continuum spectrometer was supported by a grant from the NSF (DMR-1626065).

#### References

- (1) Wigglesworth, V. B. The Use of Osmium in the Fixation and Staining of Tissues. *Proc. R. Soc. B: Biol. Sci.* **1957**, *147*, 185–199.
- (2) Kuo, J., Ed. *Electron Microscopy: Methods and Protocols*, 3rd ed.; Humana Press, 2014.
- (3) Kourkoutis, L. F.; Plitzko, J. M.; Baumeister, W. Electron Microscopy of Biological Materials at the Nanometer Scale. *Mater. Res.* **2012**, *42*, 33–58.
- (4) Svara, F.; Förster, D.; Kubo, F.; Januszewski, M.; Maschio, M. d.; Schubert, P. J.; Kornfeld, J.; Wanner, A. A.; Laurell, E.; Denk, W.; Baier, H. Automated Synapse-Level Reconstruction of Neural Circuits in the Larval Zebrafish Brain. Nat. Methods 2022, 19, 1357–1366.
- (5) Collinson, L. M. et al. Volume EM: A Quiet Revolution Takes Shape. Nat. Methods 2023, 20, 777–782.
- (6) Yin, W. et al. A Petascale Automated Iimaging Pipeline for Mapping Neuronal Circuits with High-Throughput Transmission Electron Microscopy. *Nat. Commun.* **2020**, *11*, 4949.
- (7) Subbaraman, L. R.; Subbaraman, J.; Behrman, E. J. Formation and Hydrolysis of Osmate(VI) Esters. *Inorg. Chem.* **1972**, 11, 2621–2627.
- (8) Lalaoui, N.; Reuillard, B.; Philouze, C.; Holzinger, M.; Cosnier, S.; Goff, A. L. Osmium(II) Complexes Bearing Chelating N-Heterocyclic Carbene and Pyrene-Modified Ligands: Surface Electrochemistry and Electron Transfer Mediation of Oxygen Reduction by Multicopper Enzymes. Organometallics 2016, 35, 2987– 2992.
- (9) Hua, Y.; Laserstein, P.; Helmstaedter, M. Large-Volume en-bloc Staining for Elec-

- tron Microscopy-Based Connectomics. *Nat. Commun* **2015**, *6*, 7923.
- (10) Song, K.; Feng, Z.; Helmstaedter, M. High-Contrast en bloc Staining of Mouse Whole-Brain and Human Brain Samples for EM-Based Connectomics. *Nature Methods* 2023, 20, 836–840.
- (11) Scheller, E. L.; Troiano, N.; Van-J. N.; Houtan. Bouxsein, Μ. A.; Fretz, J. A.; Xi, Y.; Nelson, T.; Katz, G.; Berry, R.; Church, C. D.; Doucette, C. R.; Rodeheffer, M. S.; MacDougald, O. A.; Rosen, C. J.; Horowitz, M. C. Use of Osmium Tetroxide Staining with Microcomputerized Tomography to Visualize and Quantify Bone Marrow Adipose Tissue in vivo. Methods Enzymol. 2014, *537*, 123–139.
- (12) Wigglesworth, V. B. Histological Staining of Lipids for the Light and Electron Microscope. *Biol. Rev.* **1988**, *63*, 417–431.
- (13) Graham, L.; Orenstein, J. M. Processing Tissue and Cells for Transmission Electron Microscopy in Diagnostic Pathology and Research. *Nat. Protoc.* **2007**, *2*, 2439– 2450.
- (14) Seligman, A. M.; Wasserkrug, H. L.; Hanker, J. S. A New Staining Method (OTO) for Enhancing Contrast of Lipid-Containing Membranes and Droplets in Osmium Tetroxide-Fixed Tissue with Osmiophilic Thiocarbohydrazide (TCH). J. Cell Biol. 1966, 30, 424–432.
- (15) Vollhardt, K. P. C.; Schore, N. E. Organic Chemistry: Structure and Function, 6th ed.; 2011.
- (16) White, D. L.; Andrews, S.; Faller, J.; Barrnett, R. J. The Chemical Nature of Osmium Tetroxide Fixation and Staining of Membranes by X-Ray Photoelectron Spectroscopy. *Biochim. Biophys. Acta Biomembr.* **1976**, 436, 577–592.
- (17) Boergens, K. M.; Wildenberg, G.; Li, R.; Lambert, L.; Moradi, A.; Stam, G.;

- Tromp, R.; Molen, S. J. v. d.; King, S. B.; Kasthuri, N. Photoemission Electron Microscopy for Connectomics. 2023.
- (18) Sun, Q.; Ueno, K.; Yu, H.; Kubo, A.; Matsuo, Y.; Misawa, H. Direct Imaging of the Near Field and Dynamics of Surface Plasmon Resonance on Gold Nanostructures Using Photoemission Electron Microscopy. *Light Sci. Appl* **2013**, 2, e118.
- (19) Dai, Y.; Zhou, Z.; Ghosh, A.; Mong, R. S. K.; Kubo, A.; Huang, C.-B.; Petek, H. Plasmonic Topological Quasiparticle on the Nanometre and Femtosecond Scales. *Nature* **2020**, *588*, 616–619.
- (20) Sun, Q.; Yu, H.; Ueno, K.; Kubo, A.; Matsuo, Y.; Misawa, H. Dissecting the Few-Femtosecond Dephasing Time of Dipole and Quadrupole Modes in Gold Nanoparticles Using Polarized Photoemission Electron Microscopy. ACS Nano 2016, 10, 3835–3842.
- (21) Joshi, P. P.; Li, R.; Spellberg, J. L.; Liang, L.; King, S. B. Nanoimaging of the Edge-Dependent Optical Polarization Anisotropy of Black Phosphorus. *Nano Lett.* 2021, 22, 3180–3186.
- (22) Man, M. K. L.; Margiolakis, A.; Deckoff-Jones, S.; Harada, T.; Wong, E. L.; Krishna, M. B. M.; Madéo, J.; Winchester, A.; Lei, S.; Vajtai, R.; Ajayan, P. M.; Dani, K. M. Imaging the Motion of Electrons Across Semiconductor Heterojunctions. Nat. Nanotechnol. 2016, 12, 36–40.
- (23) Keyshar, K.; Berg, M.; Zhang, X.; Vajtai, R.; Gupta, G.; Chan, C. K.; Beechem, T. E.; Ajayan, P. M.; Mohite, A. D.; Ohta, T. Experimental Determination of the Ionization Energies of MoSe<sub>2</sub>, WS<sub>2</sub>, and MoS<sub>2</sub> on SiO<sub>2</sub> Using Photoemission Electron Microscopy. *ACS Nano* **2017**, *11*, 8223–8230.
- (24) Li, Y.; Liu, W.; Wang, Y.; Xue, Z.; Leng, Y.-C.; Hu, A.; Yang, H.; Tan, P.-H.; Liu, Y.; Misawa, H.; Sun, Q.; Gao, Y.;

- Hu, X.; Gong, Q. Ultrafast Electron Cooling and Decay in Monolayer WS<sub>2</sub> Revealed by Time- and Energy-Resolved Photoemission Electron Microscopy. *Nano Lett.* **2020**, *20*, 3747–3753.
- (25) Neff, A.; Niefind, F.; Abel, B.; Mannsfeld, S. C. B.; Siefermann, K. R. Imaging Nanoscale Morphology of Semiconducting Polymer Films with Photoemission Electron Microscopy. Adv. Mater. 2017, 29, 1701012.
- (26) Peles, D. N.; Simon, J. D. Challenges in Applying Photoemission Electron Microscopy to Biological Systems. *Pho*tochem. Photobiol. **2009**, 85, 8–20.
- (27) Regoutz, A. et al. Insights into the Electronic Structure of OsO<sub>2</sub> Using Soft and Hard X-Ray Photoelectron Spectroscopy in Combination with Density Functional Theory. Phys. Rev. Mater. 2019, 3, 025001.
- (28) Hayakawa, Y.; Kohiki, S.; Arai, M.; Yoshikawa, H.; Fukushima, S.; Wagatsuma, K.; Oku, M.; Shoji, F. Electronic Structure and Electrical Properties of Amorphous OsO<sub>2</sub>. Phys. Rev. B **1999**, 59, 11125–11127.
- (29) Birrell, G. B.; Hedberg, K. K.; Habliston, D. L.; Griffith, O. Biological Applications of Photoelectron Imaging: a Practical Perspective. *Ultramicroscopy* 1991, 36, 235–251.
- (30) Kasthuri, N. et al. Saturated Reconstruction of a Volume of Neocortex. *Cell* **2015**, 162, 648–661.
- (31) Reinert, F.; Hüfner, S. Photoemission Spectroscopy—From Early Days to Recent Applications. *New J. Phys.* **2005**, *7*, 97–97.
- (32) Hüfner, S.; Schmidt, S.; Reinert, F. Photoelectron Spectroscopy—An Overview. Nucl. Instrum. Methods Phys. Res. A: Accel. Spectrom. Detect. Assoc. Equip. 2005, 547, 8–23.

- (33) Pignataro, M. F.; Herrera, M. G.; Dodero, V. I. Evaluation of Peptide/Protein Self-Assembly and Aggregation by Spectroscopic Methods. *Molecules* 2020, 25, 4854.
- (34) Pershina, V.; Bastug, T.; Fricke, B.; Varga, S. The Electronic Structure and Properties of Group 8 Oxides MO<sub>4</sub>, where M=Ru, Os, and Element 108, Hs. *J. Chem. Phys.* **2001**, *115*, 792–799.
- (35) Rogers, D. B.; Butler, S. R.; Shannon, R. D.; Wold, A.; Kershaw, R. Single Crystals of Transition-Metal Dioxides. *Inorg. Synth.* **2016**, 135–145.
- (36) Belazi, D.; Solé-Domènech, S.; Johansson, B.; Schalling, M.; Sjövall, P. Chemical Analysis of Osmium Tetroxide Staining in Adipose Tissue Using Imaging ToF-SIMS. *Histochem. Cell Biol.* **2009**, *132*, 105–115.
- (37) Schroeder, M. Osmium Tetraoxide cis Hydroxylation of Unsaturated Substrates. *Chem. Rev.* **1980**, *80*, 187–213.
- (38) Khan, A. A.; Riemersma, J. C.; Bbooij, H. L. The Reactions of Osmium Tetroxide with Lipids and Other Compounds. J. Histochem. Cytochem. 1961, 9, 560–563.
- (39) Nickels, J. D.; Katsaras, J. Membrane Hydration, The Role of Water in the Structure and Function of Biological Membranes. *Subcell. Biochem.* **2015**, *71*, 45–67.
- (40) Stoeckenius, W. Electron Microscopy of Fixed Lipids. *Protoplasma* **1967**, *63*, 214–217.
- (41) Cairns, J. F.; Roberts, H. L. Osmium Tetroxide-Catalysed Oxidation of Olefins. J. Chem. Soc. C 1968, 0, 640–642.
- (42) Cartwright, B. A.; Griffith, W. P.; Schröder, M.; Skapski, A. C. X-Ray Molecular Structure of the

- Asymmetrically Bridged Ester Fomplex Di- $\mu$ -oxo-bis[(cyclohexane-1,2-diolato)oxo(quinuclidine)osmium(VI)], [OsO<sub>2</sub>(O<sub>2</sub>C<sub>6</sub>H<sub>10</sub>)(C<sub>7</sub>H<sub>13</sub>N)]<sub>2</sub>. *J. Chem. Soc.* **1978**,  $\theta$ , 853–854.
- (43) Korn, E. D. A Chromatographic and Spectrophotometric Study of the Products of the Reaction of Osmium Retroxide with Unsaturated Lipids. *J. Cell Biol.* **1967**, 34, 627–638.

# **TOC** Graphic

